Article

A Multitemporal and Multilevel Land Surface Temperature Regional Attribute Change Analysis in Henan, China, Using MODIS Imagery

Zongze Zhao [1] , Bingke Sun [1], Gang Cheng [1,*], Cheng Wang [2], Na Yang [1], Hongtao Wang [1] and Xiaojie Tang [1]

1   School of Surveying and Land Information Engineering, Henan Polytechnic University, Jiaozuo 454000, China
2   Aerospace Information Research Institute, Chinese Academy of Sciences, Beijing 100094, China
*   Correspondence: chenggang@hpu.edu.cn

Abstract: Temperature is an important aspect of land–atmosphere studies and plays a key role in urban environmental change. With the continuous development of satellite remote sensing sensors, remote sensing technology has become an important means of obtaining large-scale land surface temperature (LST) data. LST can be calculated from the thermal infrared band data of remote sensing images to analyze changes in temperature and determine its relationship with the surface type. In this study, a multitemporal multilevel (MTML) method for analyzing remotely sensed LST data is presented that analyzes attribute changes and correlations of remotely sensed LST data in different periods and at different temperature levels. First, the LST data were obtained under the same climatic conditions at different times, and the influence of climatic conditions on the LST data was excluded. Threshold superposition analysis was then performed on the temperature data to generate temperature-connected regions of different levels, and a tree structure was constructed. Each node in the tree structure represented a connected region. Finally, the attribute information of different connected regions at different levels was calculated, and the attribute changes and correlations between different times and levels were analyzed. In this study, five MODIS LST datasets from 15 May 2006, 1 May 2010, 7 May 2014, 29 April 2017, and 8 May 2021 in Henan Province of China were obtained, and MTML analysis was carried out. The experimental results showed that a negative correlation exists between temperature and the vegetation index, while a positive correlation exists between temperature and the built-up index. However, with an increase in the temperature level, the correlation between temperature and the surface feature type index decreased. In addition, there were more concentrated high-temperature areas in the northern, central, and western regions of Henan Province and lower temperatures in the eastern and southern regions.

Keywords: multitemporal; multilevel; regional attribute; change analysis; land surface temperature data; Henan Province

1. Introduction

Over the past 40 years of China's reform and opening up, the urbanization process has been accelerating, from the rapid rise of eastern coastal cities and foreign trade cities to the rapid development of central and western cities. In the process of urban development, China's urban population is also increasing [1]. According to data from the National Bureau of Statistics, China's urbanization rate increased from 17.9% in 1978 to 63.9% in 2020, the number of permanent urban residents increased from 170 million in 1978 to 900 million in 2020, and the number of cities increased from 193 to 685 [2]. Rapidly growing populations drive urbanization; humans transform natural features into artificial ones that alter the surface energy and temperature conditions, destroy the urban environment, threaten biodiversity, and lead to the emergence and development of the urban heat island (UHI) effect [3–7].

The UHI effect refers to the temperature in an urban area being higher than that in the surrounding area owing to factors such as a large amount of artificial heating, high-heat storage bodies such as buildings and roads, and the reduction of green space [8–10]. In the 1960s, Manley proposed the concept of urban heat island and attracted widespread attention [11]. Later, many researchers conducted extensive studies on the distribution characteristics of UHIs [12–15]. The advent of satellite data allowed us to define a new UHI called the surface urban heat island (SUHI), which is the difference in land surface temperature (LST) between an urban area and its surrounding nonurban area [16].

In the traditional analysis method, the LST data information usually comes from the on-site measurement data of the meteorological station, but due to the limitation of the distribution points, the spatial continuous information of the whole study area is lacking, and the spatial data is affected by the measurement time. Therefore, it is difficult to analyze the spatial pattern of the UHI effect. With the development of remote sensing technology, satellite thermal data with wide spatial and temporal coverage (such as AVHRR, MODIS, Landsat TM/ETM+, and ASTER images) have been widely used for mesoscale or large-scale LST data generation and related applications during analysis and can effectively describe the spatial and temporal pattern of the thermal environment in large urban areas [17–22].

In addition, LST has a significant correlation with the distribution characteristics of ground features such as the density distribution of vegetation, water bodies, and buildings. Many researchers have conducted research and analysis on this topic. From the perspective of land type, the heat island effect mainly occurs in places where construction land is concentrated, while green space and water bodies are relatively low [23,24]. Guo et al. used Landsat data to invert NDVI, LST, and albedo products to discuss the relationship between heat flux and land use types in Beijing, which showed that green space plays an important role in mitigating the urban thermal environment [25]. Hawkins et al. studied the impact of land changes in rural areas on the spatial structures of LST data, and their analysis of the relationship between surface feature types and surface temperatures is helpful for the rational planning of land-use types [26]. Chen et al. distinguished different surface feature types by using different feature indices and applied quantitative methods to analyze the degree of correlation between temperature and feature indices [27]. Li et al. used a classification method to categorize images and temperature information to analyze the relationships among temperature changes and ground features, vegetation coverage, roads, and populations [19]. Peng et al. used satellite images to obtain the surface temperature information of Beijing to calculate the temperature distribution index of each region and analyzed the corresponding relationships among the temperature distribution index, shape of surface objects, and refractive index [1]. Zhou et al. used remotely sensed satellite images to estimate LST data and analyze the impact of vegetation cover and structure index on urban temperature distributions [9]. The above studies mainly analyzed the multitemporal variation in temperature and described its relationship with the ground object type [28,29]. However, different regions may present different temperature levels of hierarchy distribution that cannot be expressed by only multitemporal change analysis; therefore, this study proposed a multitemporal multilevel (MTML) remote sensing LST data analysis method, mainly for multiperiod remote sensing LST data, to analyze the tree structure changes of connected areas at different temperature levels and their degree of relevance with different ground object types.

Taking Henan Province as the research area, this study analyzed MODIS surface temperature product data based on the MTML temperature data analysis method. The remainder of the thesis is organized as follows: Section 2 describes the research area and data; Section 2.3 describes in detail the MTML temperature data analysis method; Sections 3 and 4 discuss and analyze the experimental results, respectively; and Section 5 is the conclusion.

2. Materials and Methods

2.1. Study Area

As shown in Figure 1, Henan Province is located in the middle and lower reaches of the Yellow River in east-central China between 31°23′ and 36°22′ north latitude and 110°21′ and 116°39′ east longitude. Henan Province has 17 prefecture-level cities, 1 county-level administrative unit, 21 county-level cities, 83 counties, and 53 municipal districts covering a total area of 167,000 square kilometers. By the end of 2020, Henan Province had a population of 99.41 million and an urban population of 25.97 million. Most of Henan Province is located in the warm temperate zone, and the south is subtropical with a continental monsoon climate that transitions from a northern subtropical to a warm temperate zone. It also has the characteristics of climate transition from east to west from plains to hills and mountains with four distinct seasons with the same period of rain and heat, complexity, and diversity, and experiences frequent climatic disasters. In the past 10 years, the annual average temperature in Henan Province has been 12.9–16.5 °C, the annual average precipitation 464.2–1193.2 mm, and the annual average hours of sunshine 1505.9–2230.7 [30].
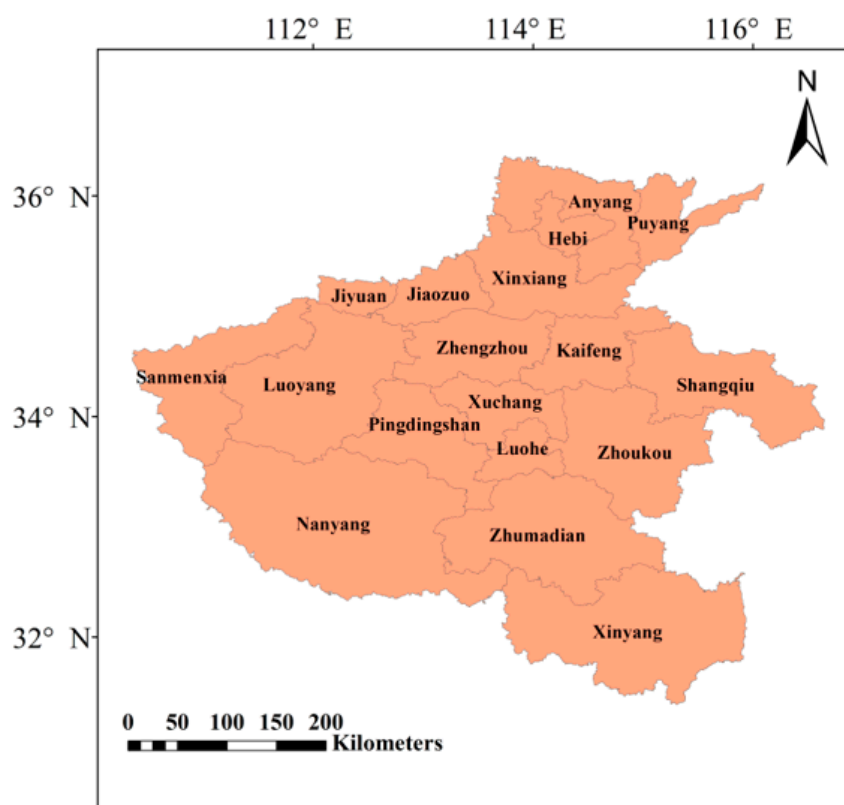

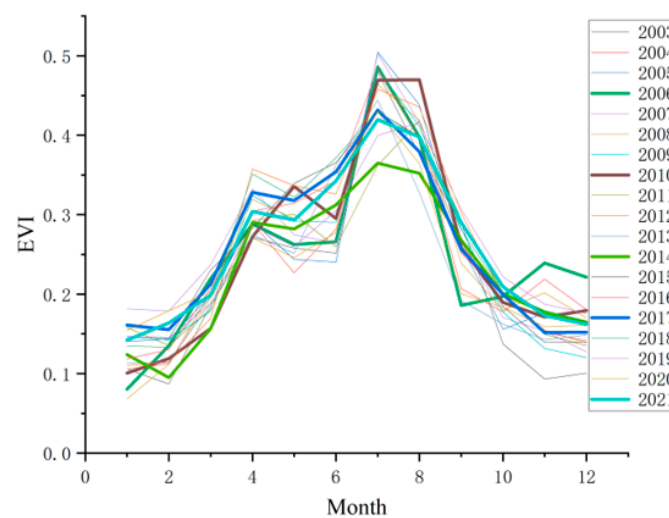**Figure 1.** Administrative map of Henan Province.

2.2. Data

In this study, two MODIS data products of the Terra satellite were selected: the MOD11_L2 surface temperature product and MOD021KM calibration radiation product, both with a spatial resolution of 1 km, and the MOD11_L2 surface temperature product with an accuracy of 1 °C [31]. All data were obtained from the National Aeronautics and Space Administration website (https://ladsweb.modaps.eosdis.nasa.gov (accessed on 21 January 2022)). Existing studies have shown that the factors affecting the surface temperature can be divided into the following categories: surface coverage type, urban landscape pattern, urban spatial form, meteorological factors, anthropogenic heat sources, etc. [32]. Among them, meteorological factors (such as temperature, precipitation, humidity, etc.) have a greater impact on the land surface temperature in terms of spatial distribution and temporal variation characteristics [33]. Therefore, in order to ensure that the types of

ground objects and climatic conditions in the acquisition time period of the multiphase images were consistent, this study analyzed the relevant information of the image data, including transit time, number of tracks and resolution, and weather conditions of the day including average temperature and average humidity. We selected the MODIS surface temperature and calibrated radiation products of 15 May 2006, 1 May 2010, 7 May 2014, 29 April 2017, and 8 May 2021 as shown in Table 1. In addition, the weather conditions were obtained from a weather data website (https://en.tutiempo.net/climate/China.html (accessed on 14 January 2022)). To compare and analyze the climate in the selected data years, taking Zhengzhou as an example, we downloaded the corresponding monthly MODIS Aqua Enhanced Vegetation Index (EVI) data from 2003 to 2021 and obtained the average monthly EVI value of Zhengzhou in each year. As shown in Figure 2a, the monthly trend of EVI values from 2003 to 2021 was plotted using line charts, and the line charts of 2006, 2010, 2014, 2017, and 2021 are shown in bold. Henan has a warm temperate subtropical, humid–semi-humid monsoon climate. Vegetation usually begins to sprout in March, branches and leaves begin to flourish in April, and leaves begin to wither in October. Therefore, this study only analyzed the climate from the end of April to the end of September in Henan Province through EVI. As shown in Figure 2a, the months with the largest EVI change in Zhengzhou from 2003 to 2021 were July and August, and the maximum change value was approximately 0.2. The maximum changes in the EVI value in April and May in 2006, 2010, 2014, 2017, and 2021 were less than 0.1. Figure 2b shows the monthly trend of the EVI standard deviations in Zhengzhou in 2006, 2010, 2014, 2017, and 2021. Among them, the EVI standard deviations in April and May were the smallest, while those of July, August, and September were the largest. Therefore, this study selected the MODIS surface temperature and calibrated radiation products for April and May of 2006, 2010, 2014, 2017, and 2021 for processing and analysis.
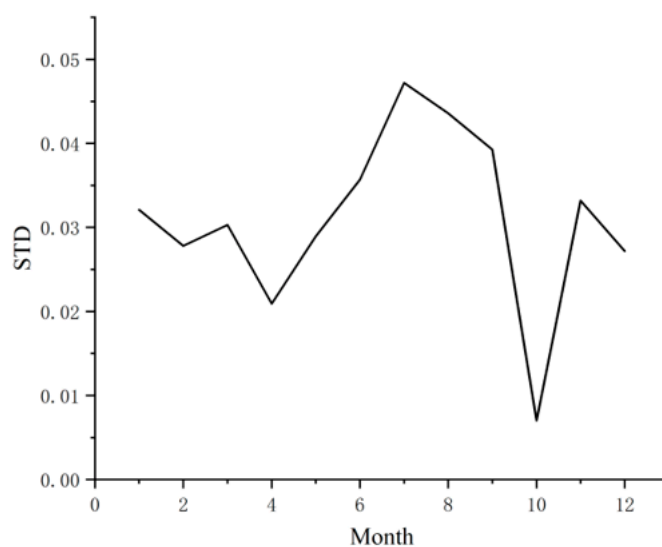
Table 1. MODIS image data list.

Number	Time	Orbital Number (Terra Satellite)	Scene-Center Time (Local Time)	Avg. Air Temperature	Humidity	Condition	Resolution (m)
1	2006-05-15	h27v05	11:20	23.7 °C	39%	Fair	1000
2	2010-05-01	h27v05	11:30	23.2 °C	59%	Fair	1000
3	2014-05-07	h27v05	11:10	25.6 °C	33%	Fair	1000
4	2017-04-29	h27v05	11:10	25.6 °C	24%	Fair	1000
5	2021-05-08	h27v05	11:20	26.7 °C	41%	Fair	1000

(a)

Figure 2. *Cont.*

(b)

Figure 2. (**a**) Line chart of EVI distribution in Zhengzhou from 2003 to 2021 by MODIS Aqua data; (**b**) line chart of EVI standard deviations in Zhengzhou in 2006, 2010, 2014, 2017, and 2021.

2.3. Methods

The method in this study can be divided into three steps: (1) LST, NDVI (normalized difference vegetation index) and NDBI (normalized difference built-up index) generated from MODIS surface temperature and calibrated radiation products; (2) connectivity analysis of LST data; and (3) MTML statistical and correlation analysis of connected regions. The technical flow chart is shown in Figure 3.

2.3.1. LST, NDVI, and NDBI Generated from MODIS Data

The MOD11_L2 surface temperature product was geometrically corrected and temperature converted, and the researched area was cropped by the EVI, and 15 May 2006, 1 May 2010, 7 May 2014, 29 April 2017, and 8 May 2021LST data were obtained for the study area.

In this study, the NDVI and NDBI were used to represent the distribution of vegetation and building feature type indices and to study their influence on LST distribution. The NDVI and NDBI were obtained by performing band arithmetic processing on multispectral data in MODIS calibration radiation products. Through the EVI, the MODIS calibration radiation products are subjected to geometric correction, calibration, and atmospheric correction preprocessing operations to obtain reflectance data and then to generate the NDVI and NDBI through band operations. The formula used to calculate the vegetation index is [34]

$$NDVI = \frac{D_{NIR} - D_R}{D_{NIR} + D_R} \tag{1}$$

where D_{NIR} and D_R are the grey values of the near-infrared and red spectral bands in the MODIS data, respectively. The built-up index, which reflects the regional distribution of built-up land, is calculated as [35]

$$NDBI = \frac{D_{SWIR} - D_{NIR}}{D_{SWIR} + D_{NIR}} \tag{2}$$

where D_{NIR} and D_{SWIR} are the near-infrared and shortwave infrared bands in the MODIS data, respectively.
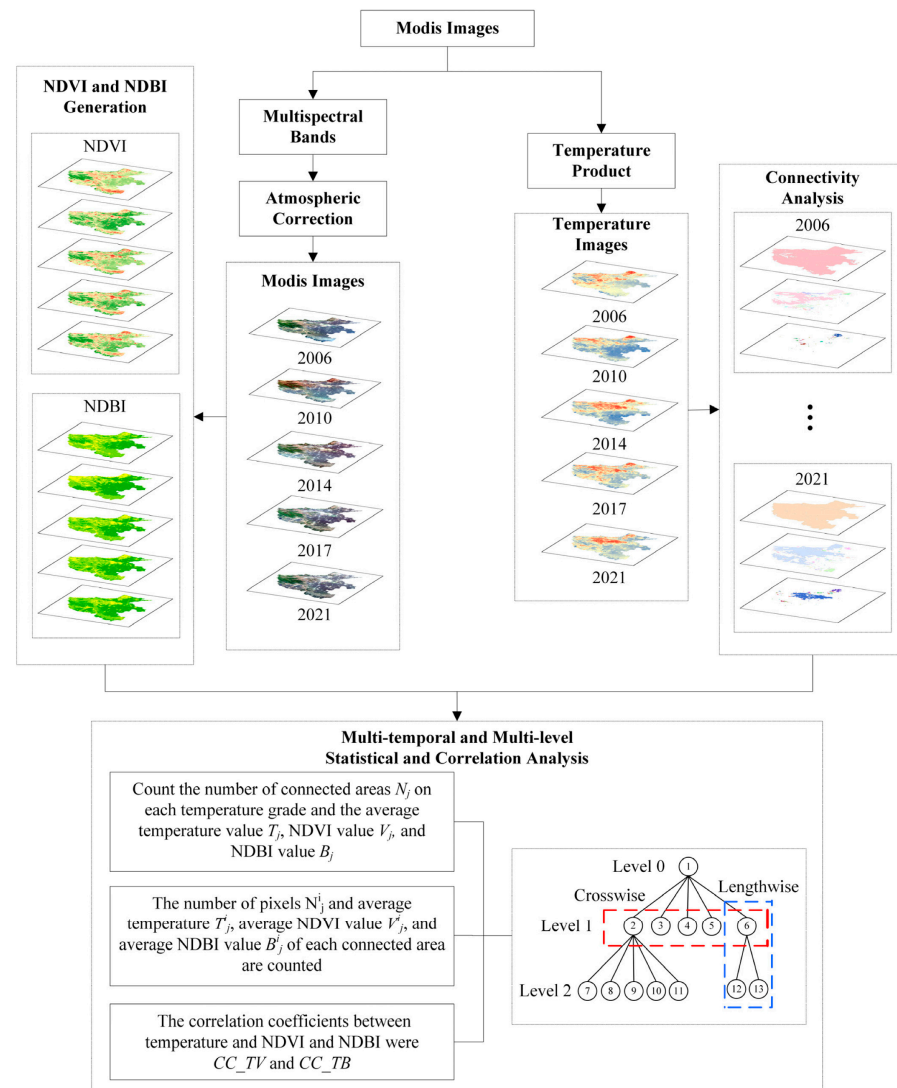
Figure 3. The technical flow chart of the paper.

2.3.2. Connectivity Analysis of LST Data

In this study, connectivity analysis was carried out on LST data. Assuming that the LST data, D, belongs to set E and that T is a threshold set $\{t_{min}..., t_i..., t_{max}\}$, the threshold set T can be used to conduct threshold superposition processing on the LST data D [36,37]; the process is

$$B_{t_i} = \{d \in E | D(d) \geq t_i\} \tag{3}$$

After processing Formula (3), the binary grid data, B, of different LST levels was obtained through the LST data.

After generating the binary grid data at different LST levels, connectivity analysis was needed. To strengthen the connectivity between the regions, the contraction-based connectivity analysis method [37] was used to analyze the connectivity of binary data at different LST levels. Thus, connected regions at different LST levels were generated. Figure 4a presents the LST data of Henan Province retrieved from the MODIS images on 7 May 2014, and Figure 4b–d show the connected regions generated by the LST data at different temperature levels.

2.3.3. MTML Attribute Information Statistics and Correlation Analyses

To analyze the relationship between the LST data and the ground-object-type index of the connected areas at different LST levels, this study generated binary grid data at different levels from 25 °C to 40 °C at 1 °C intervals and then conducted connectivity analyses to generate connected regions. After the connected regions were generated, the attribute information of each connected region was counted.
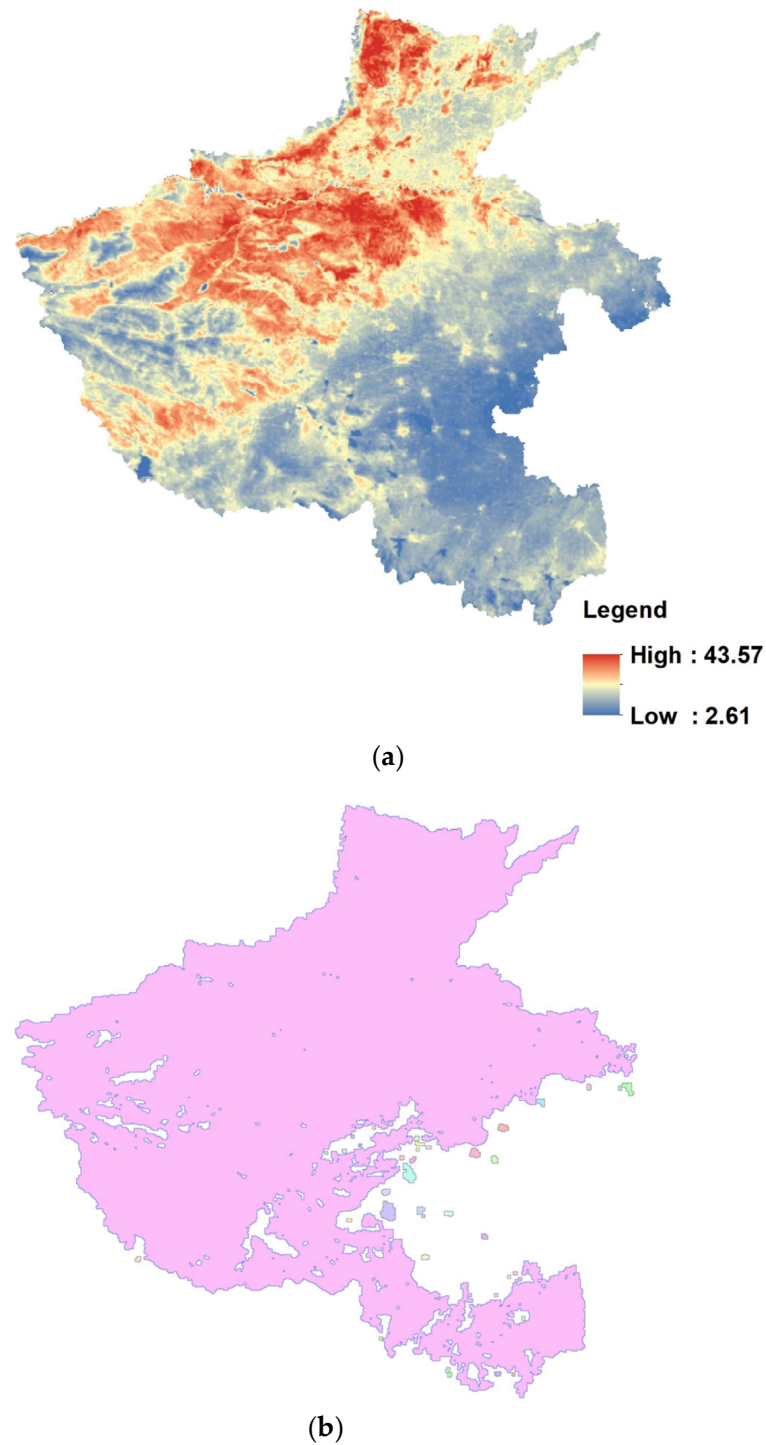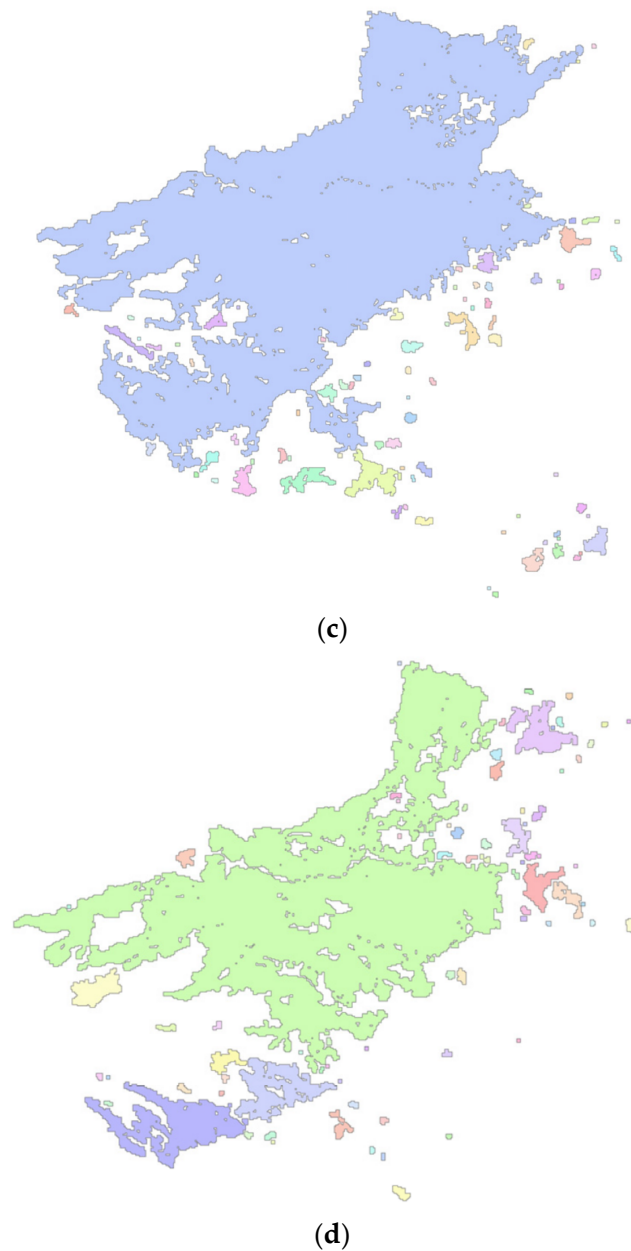

(**a**)

(**b**)

Figure 4. *Cont.*

(**c**)

(**d**)

Figure 4. Connectivity analysis of LST data retrieved from MODIS image on 7 May 2014: (**a**) LST data retrieved from MODIS images, and (**b**–**d**) connected regions generated by the LST data at temperature levels of 25, 28, and 31 °C, respectively (colors represent separate connected regions).

Let C_j^i be the ith connected region at the jth temperature level and N_j^i be the number of pixels in region C_j^i. The term N_j represents the number of connected regions (NC) at the jth temperature level. As shown in Table 2, the average LST (AT) T_j^i, NDVI (AV) V_j^i, and NDBI (AB) B_j^i values were calculated for the ith connected region at the jth temperature level to analyze the relationship between the LST and ground-object-type index values of the connected regions at different temperature levels. Therefore, the average values of LST, NDVI, and NDBI (T_j, V_j, and B_j) of all connected regions at each temperature level were calculated to analyze the correlation of LST and ground object types at different temperature levels.

Table 2. List of attribute information of connected regions.

Category	Description	Equation
Size and number of one connected region and number of connected regions at one level	Pixel number of *i*th connected region at *j*th temperature level;number of connected regions at *j*th level	N_j^i, N_j,
Mean LST of one connected region	Average LST of *i*th connected region at *j*th temperature level	$T_j^i = \frac{\sum_{k=1}^{N_j^i} LST_k}{N_j^i}$
Mean NDVI of one connected region	Average NDVI of *i*th connected region at *j*th temperature level	$V_j^i = \frac{\sum_{k=1}^{N_j^i} NDVI_k}{N_j^i}$
Mean NDBI of one connected region	Average NDBI of *i*th connected region at *j*th temperature level	$B_j^i = \frac{\sum_{k=1}^{N_j^i} NDBI_k}{N_j^i}$
Mean LST at one level	Average LST of all connected regions at *j*th temperature level	$T_j = \frac{\sum_{i=1}^{N_j} T_j^i}{N_j}$
Mean NDVI at one level	Average NDVI of all connected regions at *j*th temperature level	$V_j = \frac{\sum_{i=1}^{N_j} V_j^i}{N_j}$
Mean NDBI at one level	Average NDBI of all connected regions at *j*th temperature level	$B_j = \frac{\sum_{i=1}^{N_j} B_j^i}{N_j}$
Correlation coefficient	Correlation coefficients of LST and NDVI and LST and NDBI	CC_TV, CC_TB

The correlation between the LST and the ground object index is expressed by calculating the correlation coefficient between them. The correlation coefficient is calculated as

$$CC\_XY = \frac{Cov(X,Y)}{\sqrt{Var(X) \times Var(Y)}} \tag{4}$$

In Formula (4), *X* and *Y* are two datasets, *Cov(X, Y)* is their covariance, and *Var(X)* and *Var(Y)* are their variances. Then, we assumed that *CC_TV* is the correlation coefficient of LST and NDVI, and *CC_TB* that of LST and NDBI.

In addition, this study analyzed the changes in connected areas in different cities at different temperature levels by constructing a maximum tree structure; that is, constructing tree nodes of connected areas according to the inclusion relationship of connected areas at different temperature levels [38]. Figure 5a–c shows the connected areas generated at various LST levels in Sanmenxia city, Henan Province, in 2006. The connected areas circled in red at the first LST level of 25 °C (Figure 5a) generated new connected areas at 26 °C and 27 °C (Figure 5b,c), which can be represented by a maximum tree structure (Figure 5d) in which the nodes at a certain level of the tree structure represent a connected region at this level. Therefore, after generating the connected areas at different LST levels of prefecture-level cities in Henan Province, the tree structure was generated, and the temperature spatial structure distribution was analyzed according to the structure.

As shown in Figure 5d, all nodes can be retrieved crosswise and lengthwise in the tree structure, where the red and blue dashed rectangles represent "retrieving crosswise" and "retrieving lengthwise", respectively, and one node represents a connected region at a certain temperature level. The maximum number of horizontal nodes in the tree structure can be obtained by crosswise searching nodes, and the number of nodes in the first few layers of the tree structure shows the number of urban surface temperature centers. The maximum number of layers of a temperature center in the tree structure can be obtained by lengthwise searching nodes that reflect the vertical depth of the temperature center. A large number of horizontal nodes in a city means that there are multiple temperature radiation centers in the city, and the surface temperature is easier to diffuse. The presence of a large number of vertical layers in a city's temperature radiation center means that the temperature center is more likely to produce high-temperature areas.
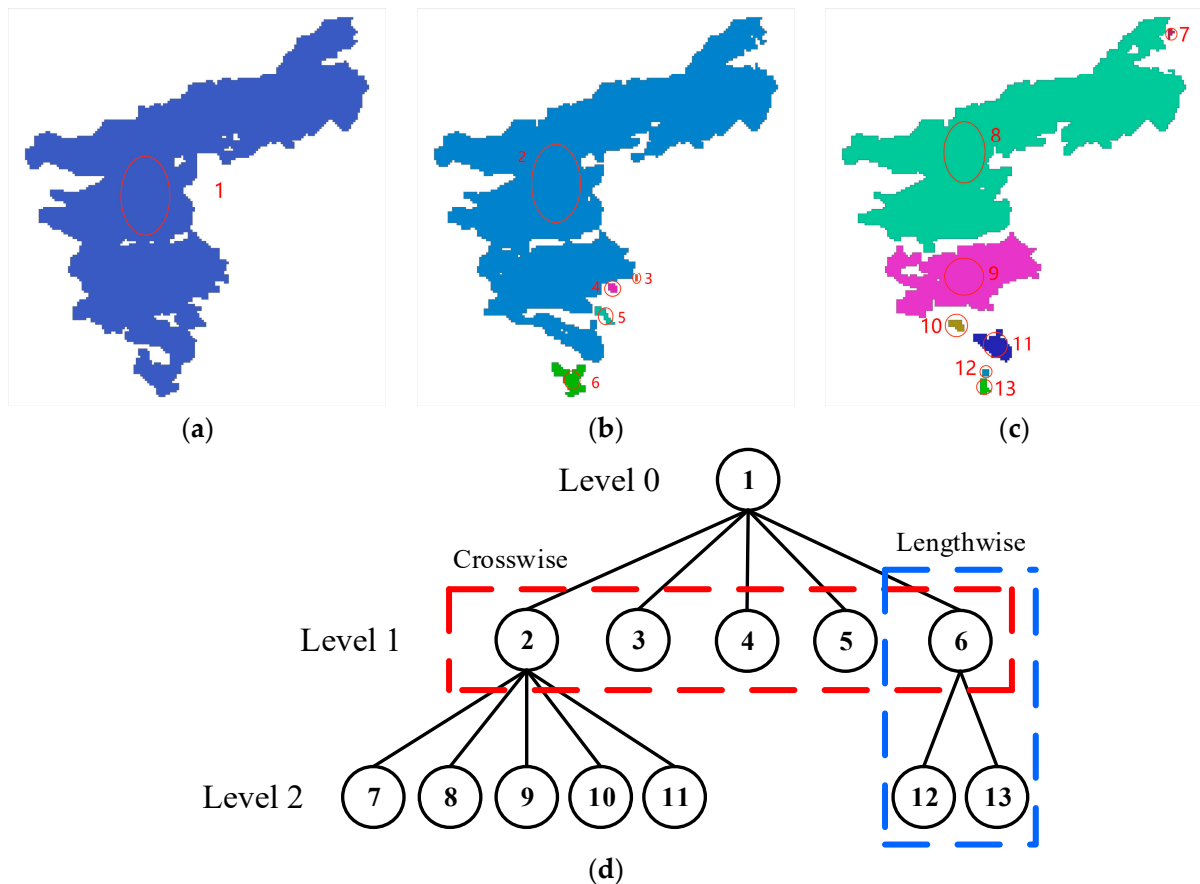
Figure 5. (**a**–**c**) represent the analysis results of the first-, second- and third-level connected regions, respectively, and (**d**) shows the tree structure construction. The numbers in (**a**–**d**) represent the label of a separate area, respectively. The red and blue dashed rectangles in Figure 5d represent "retrieving crosswise" and "retrieving lengthwise" of the tree structure, respectively.

3. Results

3.1. LST and Feature-Type Index Values Generated from MODIS Data

LST data were obtained from the MODIS LST products on 15 May 2006, 1 May 2010, 7 May 2014, 29 April 2017, and 8 May 2021, the NDVI and NDBI data were obtained from MODIS calibrated radiation products. Figures 6–8 plot the LST, NDVI, and NDBI grading maps for five dates in Henan Province, respectively. As shown in Table 3, the average temperature on 29 April 2017 was the highest, the average temperature on 1 May 2010 was the lowest, and the standard deviation of the LST data on 7 May 2014 was greater than those on 15 May 2006, 1 May 2010, 29 April 2017, and 8 May 2021. This indicates that on 7 May 2014, the surface temperature in Henan Province was high and the temperature range was wide, while on 1 May 2010, the surface temperature was low and the temperature range small. The average NDVI values on 15 May 2006, 1 May 2010, 7 May 2014 were smaller than those on 29 April 2017 and 8 May, while the standard deviation of the NDVI data on 8 May 2021 was larger than those of other years. The average NDBI value on 8 May 2021 was less than that on 15 May 2006, 1 May 2010, 7 May 2014, and 29 April 2017. The mean NDBI values varied the most from 15 May 2006 to 1 May 2010, and the standard deviation of NDBI data on 1 May 2010 was the largest. This indicates that significant changes in land use occurred in Henan Province in 2010, resulting in a significant decrease in NDBI. The NDVI value in Henan Province also increased in 2010, indicating that relevant decision-making departments gradually began to pay attention to ecological environmental protection.
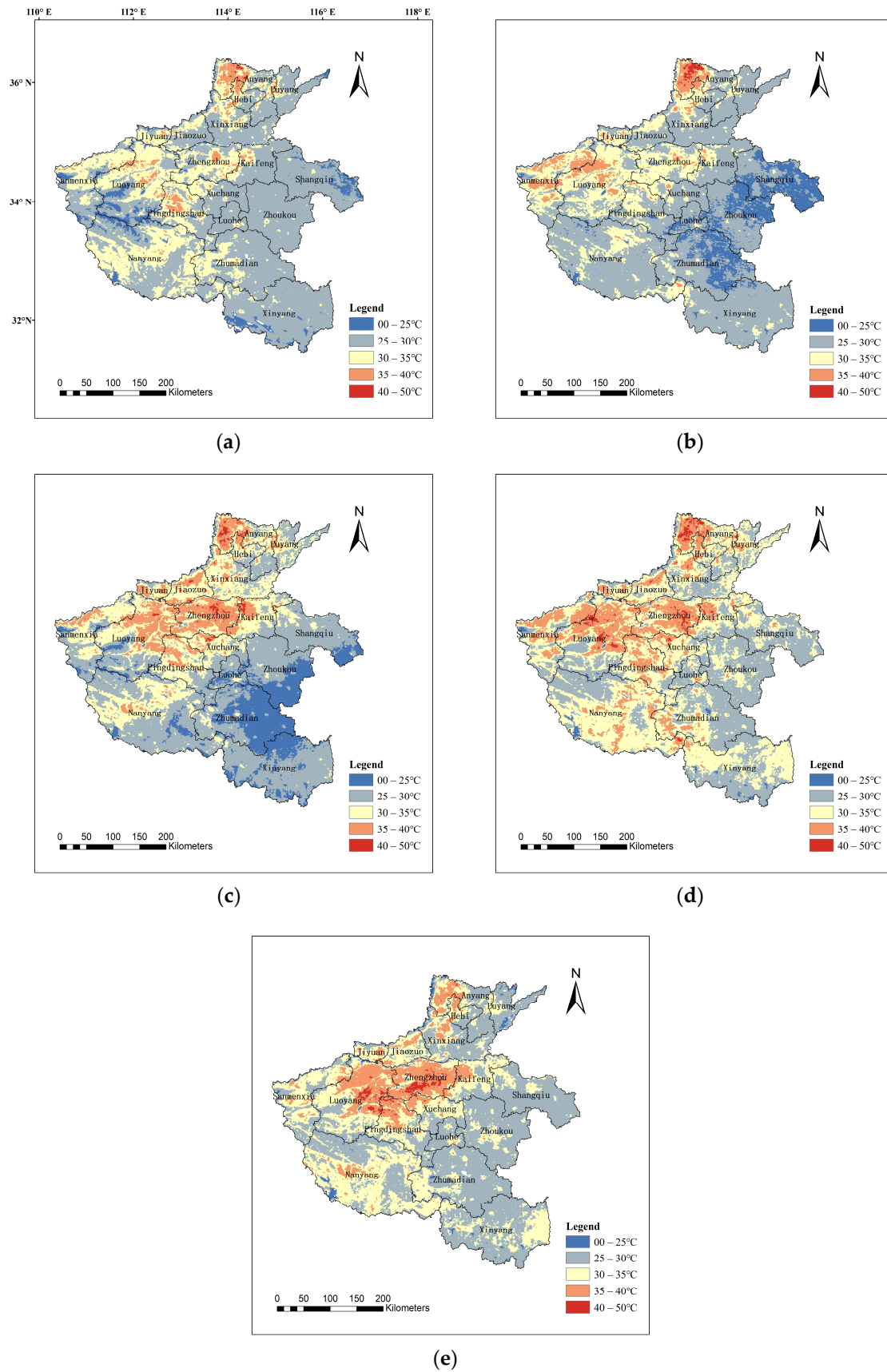
Figure 6. LST distributions on: (**a**) 15 May 2006, (**b**) 1 May 2010, (**c**) 7 May 2014, (**d**) 29 April 2017, and (**e**) 8 May 2021.

(**a**)

(**b**)

(**c**)

(**d**)

(**e**)

Figure 7. NDVI distributions on: (**a**) 15 May 2006, (**b**) 1 May 2010, (**c**) 7 May 2014, (**d**) 29 April 2017, and (**e**) 8 May 2021.

Figure 8. NDBI distributions on: (**a**) 15 May 2006, (**b**) 1 May 2010, (**c**) 7 May 2014, (**d**) 29 April 2017, and (**e**) 8 May 2021.

Table 3. Average LST, NDVI, and NDBI values of connected regions on five dates.

Attribute	Year	Minimum	Maximum	Mean	Standard Deviation
LST	2006-05-15	0.27	43.43	29.03	2.91
	2010-05-01	1.53	45.11	28.45	3.33
	2014-05-07	2.61	43.57	29.39	4.24
	2017-04-29	2.85	45.17	31.57	3.34
	2021-05-08	0.51	44.13	30.63	3.46
NDVI	2006-05-15	−0.2720	0.8963	0.5779	0.1393
	2010-05-01	−0.3902	0.8555	0.6044	0.1286
	2014-05-07	−0.1380	0.9024	0.5784	0.1320
	2017-04-29	−0.2953	0.8998	0.6335	0.1411
	2021-05-08	−0.2189	0.9568	0.6548	0.1501
NDBI	2006-05-15	−0.5751	0.1192	−0.2182	0.1041
	2010-05-01	−0.5516	0.1270	−0.2717	0.1493
	2014-05-07	−0.4880	0.1050	−0.2311	0.1123
	2017-04-29	−0.6016	0.1035	−0.2524	0.1318
	2021-05-08	−0.5577	0.1092	−0.2750	0.1295

Combining Table 3 and Figures 6–8 we can see that from 15 May 2006 to 1 May 2010, the average NDVI value increased, while the average NDBI value decreased, resulting in a decrease in the average LST. During this period, NDVI decreased and NDBI increased in Anyang, Sanmenxia, and Luoyang, resulting in an increase in high temperature areas. However, in Pingdingshan, Nanyang, and Zhumadian, NDVI increased and NDBI decreased, resulting in a large reduction in high temperature areas. Shangqiu and Zhoukou also had relatively obvious cooling, which was related to the decline of regional NDBI. From 1 May 2010 to 7 May 2014, the average NDVI value decreased and the average NDBI value increased, resulting in an increase in the average LST. During this period, the high temperature areas in northern and central Henan Province increased significantly, especially in Zhengzhou, Luoyang, and some surrounding areas; the high temperature reached above 35 °C. Areas where the surface temperature of Xinyang reaches above 30 °C also increased significantly. As can be seen from Figures 7 and 8, NDVI decreased and NDBI increased in these areas. However, there is no obvious warming phenomenon in southeastern Henan Province. From 7 May 2014 to 8 May 2021, although the average NDVI value increased and the average NDBI value decreased, the average LST still increased, reaching more than 30 degrees, indicating that the effects of vegetation and building features on temperature gradually weaken. This change needs to attract the attention of relevant decision-making departments. However, it is worth noting that from 2017 to 2021, except for Anyang, Zhengzhou, Luoyang, and Pingdingshan areas where there are still large areas of high temperature areas, the high temperature areas above 35 °C in other cities have decreased.

3.2. Connectivity Analysis of LST Data

A connectivity analysis of LST data on the five dates studied in Henan Province was carried out. First, threshold superposition analysis was performed on the LST data from 25 to 40 °C to generate binary image data at different LST levels. Then, connectivity analysis was performed on the binary image data at each LST level for the five dates to generate connected regions and count the number of connected regions and determine the degree of fragmentation at each LST level. The degree of fragmentation reflects the complexity of the spatial structure of a segmented area. The concept comes from the degree of fragmentation of the landscape [39]. The calculation process used to determine regional fragmentation (RF), P, is

$$P = \frac{N_j}{\sum\limits_{i=1}^{N_j} N_j^i} \tag{5}$$

Figure 9 shows the changes in the number of connected regions and their degree of fragmentation at each LST level in Henan Province for five dates. On the whole, with an increase in temperature, the number of connected regions first increased and then decreased, and the regional fragmentation increased continuously. As shown in Figure 9a, in 2006 and 2021, the number of connected regions reached peaks at 31 and 32 °C, respectively. In 2010, the number of connected regions peaked at 137 at 30 °C. In 2014, the number of connected regions peaked at 29, 33, and 35 °C. In 2017, the number of connected regions peaked at 30, 32, and 35 °C. The peaks on all five dates were between 29 and 35 °C, indicating that there were more heat island areas in the study area in this temperature range. The results show that the peak point of the number of connected regions was the lowest on 7 May 2014. When the LST reached 30 °C, the number of connected regions on 8 May 2021, reached the maximum among the five dates, but the degree of regional fragmentation was smaller, indicating that the area reaching 30 °C in Henan Province during this period was relatively compact and large. On 29 April 2017, when the number of connected regions reached a peak, the temperature was the highest, and the degree of regional fragmentation was smaller, indicating that there were many high-temperature areas in Henan Province during this period that were relatively compact, and the range of high-temperature areas was relatively large. In 2006, the high-temperature area had the largest fragmentation degree, but the number of connected regions was small, indicating that the number of high-temperature areas in Henan Province was little and relatively scattered during this period and the high-temperature areas were small in scope.
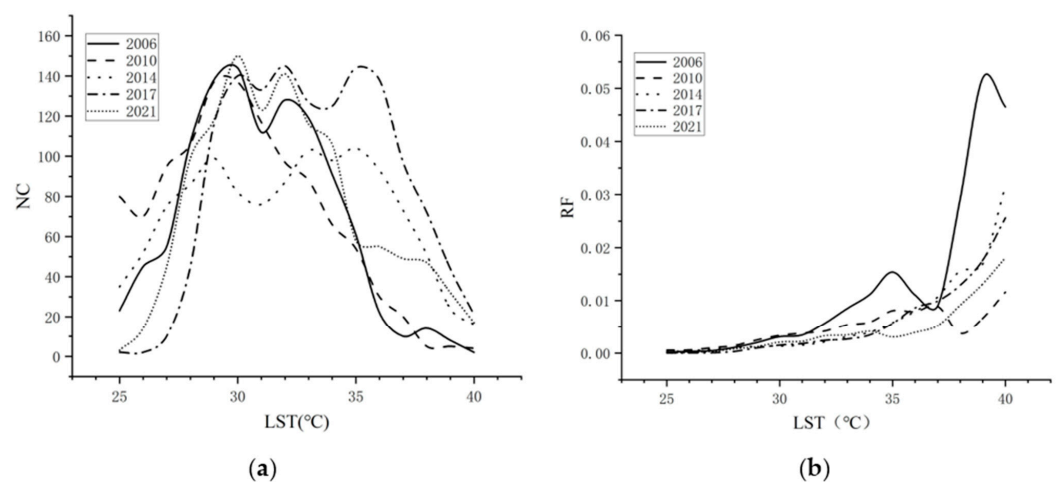

Figure 9. LST distribution curves on five dates according to (**a**) number of connected regions (NC) and (**b**) regional fragmentation (RF).

Figure 10a–e shows the distribution maps of the connected regions at the 35 °C level in the LST data of Henan Province on five dates. As shown in Figure 10, from 15 May 2006, to 1 May 2010, there were many high-temperature areas in Anyang, Luoyang, Sanmenxia, and Xinxiang; Zhengzhou and Kaifeng also experienced high temperatures in small areas, and the high-temperature areas in Pingdingshan decreased significantly. From 1 May 2010, to 29 April 2017, the high-temperature regions in Henan Province continued to increase. In 2017, the average LST of Henan Province reached the highest value, particularly, Anyang, Zhengzhou, and its surrounding urban areas, which formed a relatively dense high-temperature region, and Nanyang and Zhumadian also added more high-temperature connected areas. From 29 April 2017 to 8 May 2021, Zhengzhou and its surrounding urban areas formed more intensive high-temperature areas, while the high-temperature areas in Zhumadian, Sanmenxia, Luohe, and Nanyang began to decrease. Overall, the high-temperature regions in Henan Province are mainly distributed in the northern, central, and western regions, while the eastern and southern regions have fewer high-temperature regions.
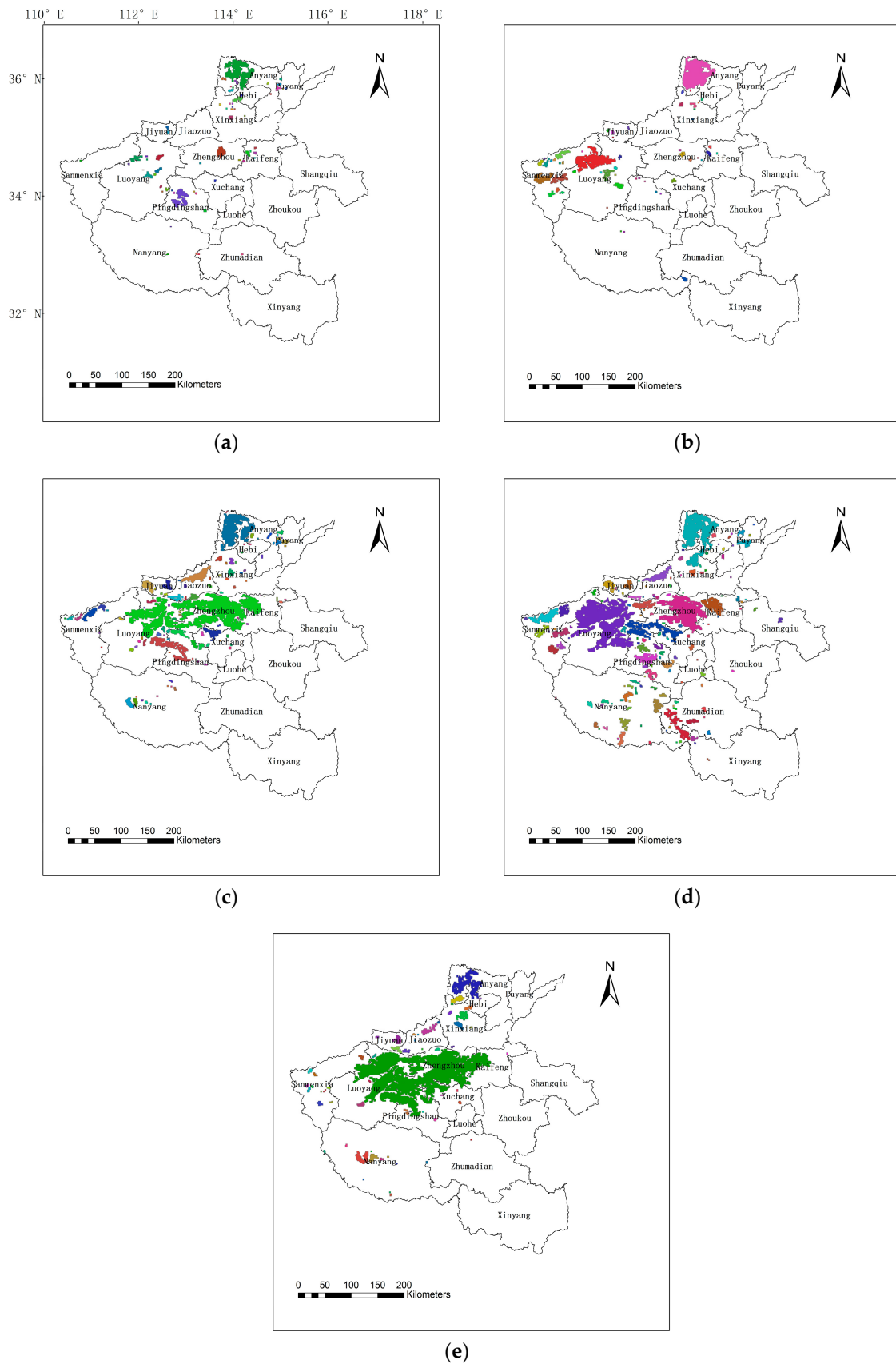
Figure 10. Distribution maps of connected regions at 35 °C level on: (**a**) 15 May 2006, (**b**) 1 May 2010, (**c**) 7 May 2014, (**d**) 29 April 2017, and (**e**) 8 May 2021.

3.3. Statistical and Correlation Analysis of Connected Regions

To analyze the relationship between the LST changes and surface-object-type index values in the connected regions at different temperature levels, attribute information, including the LST and surface-object-type index values of connected regions, should be calculated statistically. Therefore, the average LST, NDVI, and NDBI values of all connected areas at each temperature level on the five dates in Henan were calculated.

To perform a quantitative analysis of the correlation between the LST distribution and the surface-feature-type index, the correlation coefficients CC_TV representing the correlation of the average LST and average NDVI and CC_TB representing the correlation of the average LST and NDBI values of all connected regions at different temperature levels were calculated.

Figure 11a–c shows the changes in the average LST, NDVI, and NDBI in the connected regions of each temperature level in Henan Province on five dates, respectively. When the temperature was higher than 30 °C, with an increase in the average LST, the average NDVI decreased while the average NDBI increased. Because the number of connected regions at the 25–26 °C temperature level in 2017 and 2021 was less than that in other years, the average LST at this level in 2017 and 2021 was higher than that in other years. At 26–27 °C, the average NDVI increased and the average NDBI decreased on 29 April 2017; therefore, the average LST decreased at this temperature level. At 25-26 °C, the average NDVI and NDBI decreased on 8 May 2021, while the average LST decreased. The average NDVI values on 29 April 2017, and 8 May 2021, were close and higher than those on the other three dates (Figure 11b), while the average NDBI values were lower than those on the other three dates (Figure 11c), indicating that with rapid development, much greening work had been done to protect the ecological environment in Henan Province. The average NDBI on 8 May 2021, was higher than that on 29 April 2017, indicating that with the development of cities, the built-up areas in Henan Province became denser between 2017 and 2021, leading to an increase in NDBI. Judging from the change trends of the NDVI and NDBI, compared with other years, 2017 and 2021 had higher NDVIs and lower NDBIs at the same temperature level, indicating that the influence of vegetation and building types on the LST in Henan Province was gradually weakening.
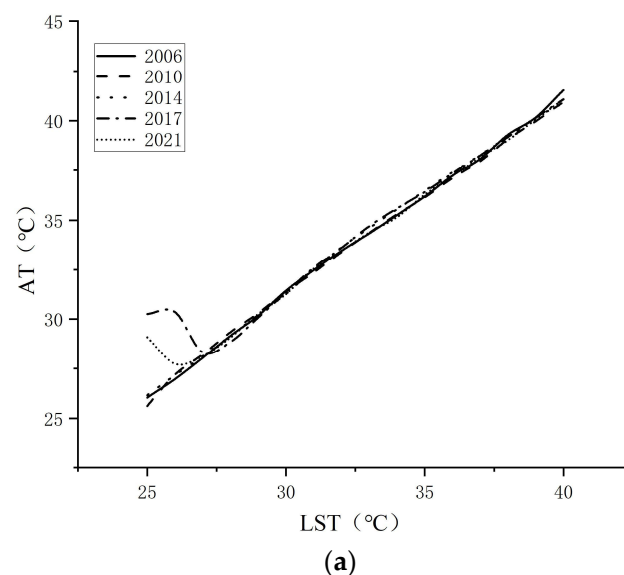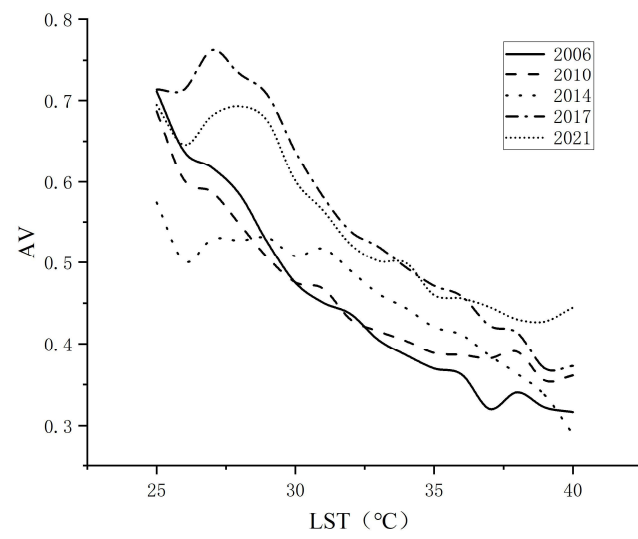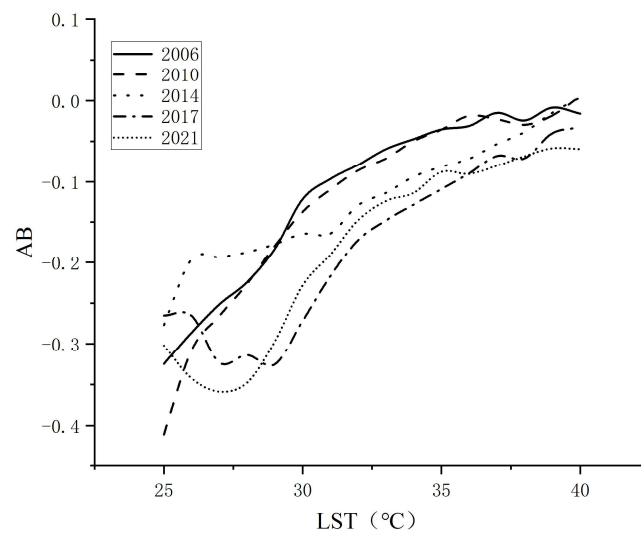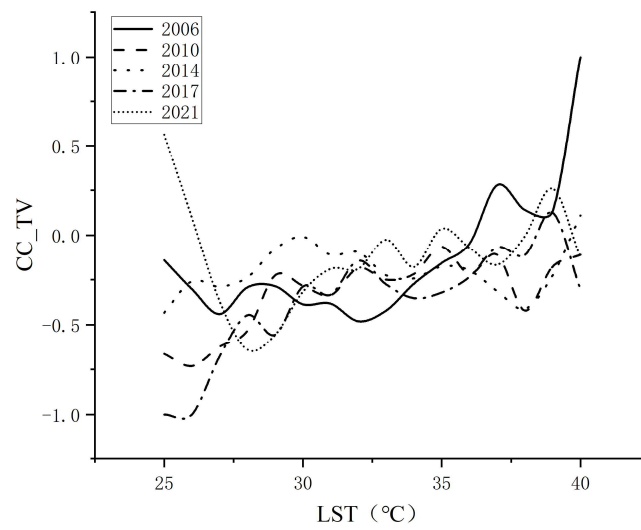

(a)

Figure 11. *Cont.*

(b)

(c)
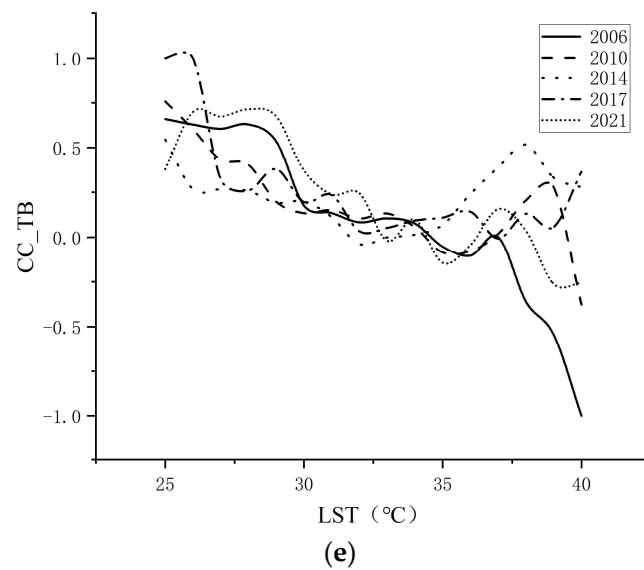

(d)

Figure 11. *Cont.*

Figure 11. Distribution curves of attribute information of connected regions on five dates: (**a**) average LST, (**b**) average NDVI, (**c**) average NDBI, and correlation coefficients of LST, (**d**) NDVI, and (**e**) NDBI.

At different LST levels, the average temperatures were negatively correlated with the NDVI values of connected areas at the beginning (Figure 11b) and positively correlated with the average NDBI values (Figure 11c). However, with an increase in temperature, the correlations between the temperature values and the NDVI and NDBI values decreased. This indicates that the distributions of NDVI and NDBI in connected regions at low-temperature levels had obvious change trends and were strongly correlated with temperature, while with an increase in temperature, the NDVI and NDBI in connected regions at high-temperature levels tended to be unstable, and their correlations with temperature decreased. In addition, the CC_TV and CC_TB on all dates exhibited an increasing trend in the high-temperature range.

4. Discussion

4.1. Influence of Connected Region Size

In general, the statistics regarding the attributes of connected regions were affected by the size of each region. If the size of a region is sufficiently small, the attribute information of that region will be vulnerable to the influences of individual pixels and will lack stability, while the attribute statistics of large regions are relatively stable and can be analyzed for trends in the attribute information. Therefore, this section analyzes the influence of region size on the attribute statistics of connected regions at 35 °C.

As shown in Table 4, the attribute information of the connected regions of each temperature level on the five study dates of different area ranges were analyzed, including the number of regions, regional fragmentation, and average LST, NDVI and NDBI, and the CC_TV and CC_TB were calculated.

Table 4. Attribute information of connected regions with different area sizes on five dates.

Date	Size (Pixels)	NC	RF	AT (°C)	AV	AB	CC_TV	CC_TB
	1–10	20	0.1111	33.41	0.4267	−0.0763	−0.4391	−0.0718
	11–30	47	0.0545	33.26	0.4404	−0.0841	−0.6488	0.1781
2006-05-15	31–60	23	0.0230	33.33	0.4317	−0.0833	−0.3862	−0.0736
	>60	38	0.0019	33.82	0.4398	−0.0722	−0.4258	0.0036

Table 4. *Cont.*

Date	Size (Pixels)	NC	RF	AT (°C)	AV	AB	CC_TV	CC_TB
2010-05-01	1–10	25	0.1111	32.86	0.4519	−0.0786	−0.6124	0.3263
	11–30	36	0.0558	33.40	0.4077	−0.0877	−0.1623	0.0204
	31–60	8	0.0251	33.35	0.4615	−0.1208	0.0461	0.4268
	>60	28	0.0013	33.88	0.4297	−0.0812	0.0326	0.1785
2014-05-07	1–10	17	0.1111	33.20	0.4987	−0.1402	−0.0003	0.1282
	11–30	33	0.0520	33.40	0.4789	−0.1243	0.0724	−0.3213
	31–60	10	0.0228	33.92	0.5144	−0.1544	−0.4923	0.0723
	>60	27	0.0007	34.08	0.4875	−0.1186	−0.3574	0.1008
2017-04-29	1–10	26	0.1111	33.29	0.5754	−0.1902	−0.3135	0.3660
	11–30	59	0.0534	33.31	0.5389	−0.1766	−0.0343	−0.1283
	31–60	31	0.0235	33.80	0.5271	−0.1728	−0.0425	−0.2955
	>60	29	0.0005	34.28	0.5166	−0.1481	0.0132	−0.1158
2021-05-08	1–10	31	0.1111	33.05	0.5557	−0.1732	−0.4759	0.4153
	11–30	47	0.0547	33.34	0.5216	−0.1472	−0.0238	0.1033
	31–60	26	0.0252	33.49	0.4951	−0.1314	−0.1498	0.2374
	>60	37	0.0009	33.94	0.5139	−0.1385	−0.1167	0.0710

Note: NC: number of connected regions; RF: regional fragmentation; AT: average LST; AV: average NDVI; AB: average NDBI; CC_TV: correlation coefficient of temperature and NDVI; CC_TB: correlation coefficient of temperature and NDBI.

According to their area size (in pixels), the connected areas were divided into four grades: 1–10, 11–30, 31–60, and greater than 60. According to the data analysis presented in Table 4, with an increase in the regional size, the average LST varied within 1 °C, basically presenting a gradual upwards trend, while the average NDVI and NDBI exhibited little change. On the five study dates, the number of connected regions first increased, then decreased, and then increased with an increase in the regional size, and the regional fragmentation always decreased. When the area size was 11–30, the number of connected regions was the largest, and the regional fragmentation was larger. When the area size was greater than 60, the number of connected regions was second only to that of the range 11–30, but the regional fragmentation was the lowest. In addition, the CC_TV was negatively correlated in 2006 and 2021 but positively correlated in some areas in 2010, 2014, and 2017. The CC_TB was positively correlated in 2010 and 2021 but negatively correlated in some areas in 2006, 2014, and 2017. In view of these abnormal situations, this study combined the analysis of on-site features (Figure 12) to obtain the following typical explanations. When NDVI was large, LST was high because the connected regions were located in mountainous areas with wide surrounding vegetation coverage, but there were clustered residential areas in the connected regions (Figure 12a). Furthermore, in the connected regions, farmland and aggregated buildings intersected (Figure 12b), and both buildings and human activities caused the LST to rise. When the NDVI was small, the LST was low because the connected regions were located in an urban area, but there were large areas of farmland with surrounding water; therefore, the LST was low (Figure 12c). Furthermore, although there were terraces without vegetation coverage in the connected regions, there was a large surrounding area of mountain forests that led to a low LST (Figure 12d). When the NDBI was larger, the LST was lower owing to the presence of more buildings in the connected regions, but a large amount of farmland around the buildings led to a lower LST (Figure 12e,f).
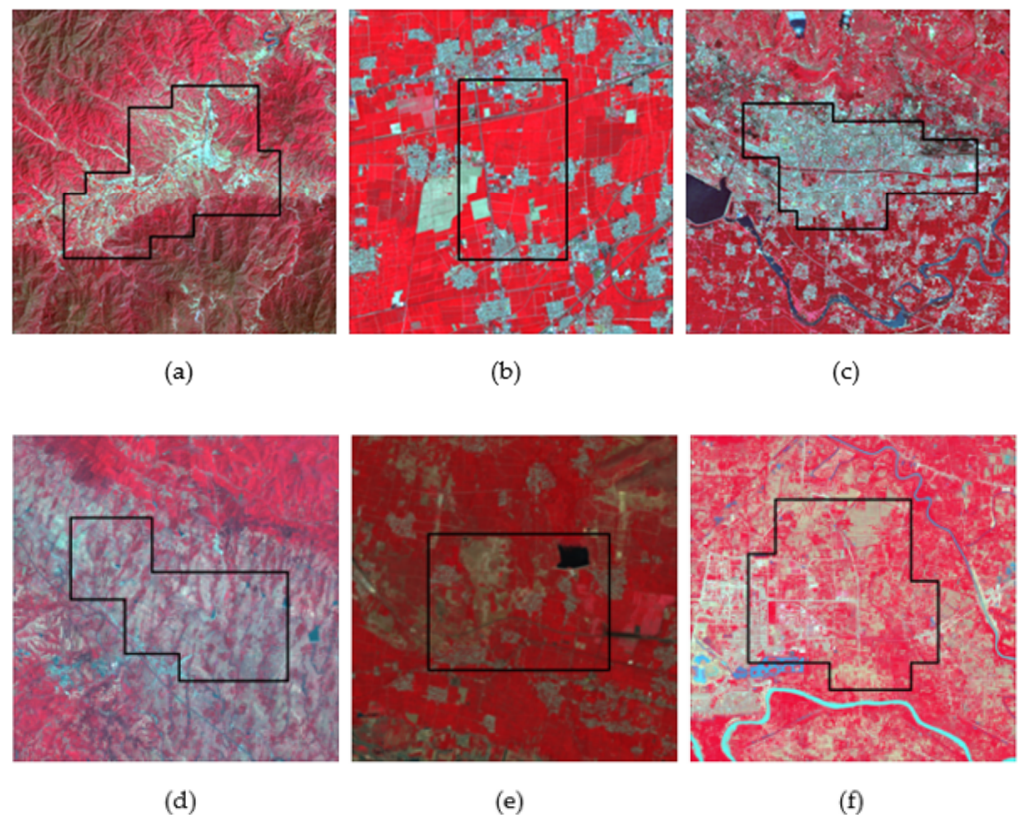
Figure 12. (**a**–**f**) are false-color image maps representing typical regions of abnormal correlation coefficients, respectively. The black box in each figure is the connected area with abnormal correlation coefficient.

4.2. Properties of High LST Regions in Different Districts

To analyze the LST variation properties of different regions in Henan Province, seven cities with different levels were selected according to the new classification list of Chinese cities released by "China Business News" in 2020; namely, Zhengzhou, Luoyang, Xinxiang, Kaifeng, Anyang, Hebi, and Sanmenxia. Statistical analysis was performed on the number of connected regions, regional fragmentation, average LST, average NDVI, average NDBI, and correlation coefficients of seven cities in Henan Province with temperature grades above 35 °C.

As shown in Figure 13, Luoyang, Sanmenxia and Xinxiang have a greater number of high-temperature connected regions, while Anyang, Zhengzhou, and Kaifeng have relatively few high-temperature connected regions, and Hebi has the fewest. From 15 May 2006 to 8 May 2021, the number of connected regions in Zhengzhou first increased and then decreased, and the number of connected regions in Sanmenxia first increased, then decreased, and then increased. The number of connected regions in the other cities first decreased, then increased, and then decreased. In addition, compared with other cities, the number of connected regions between Anyang and Hebi was extremely small on 1 May 2010, and the number of connected regions between Zhengzhou and Anyang on 8 May 2021, also reached a minimum. Except for Zhengzhou, the regional fragmentation of other cities decreased significantly from 15 May 2006 to 1 May 2010. From 1 May 2010, to 7 May 2014, the regional fragmentations of Zhengzhou, Luoyang, Kaifeng, and Xinxiang decreased, while that of Anyang, Hebi, and Sanmenxia increased. From 7 May 2014 to 29 April 2017, the regional fragmentations of Zhengzhou and Kaifeng increased, and those of other cities decreased to varying degrees. From 29 April 2017 to 8 May 2021, with the exception of Sanmenxia and Hebi where regional fragmentation increased, the remainder of the cities decreased but changed little.
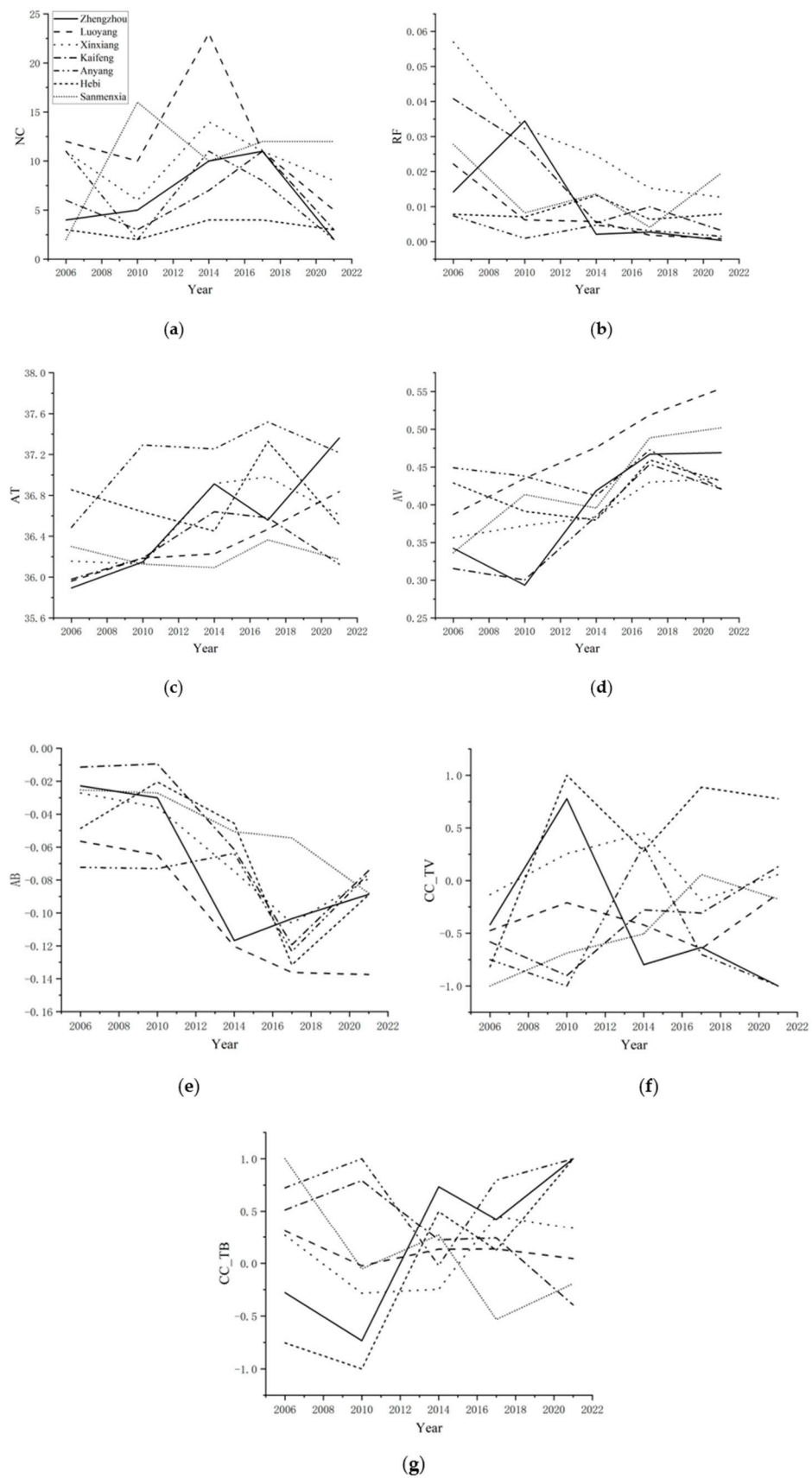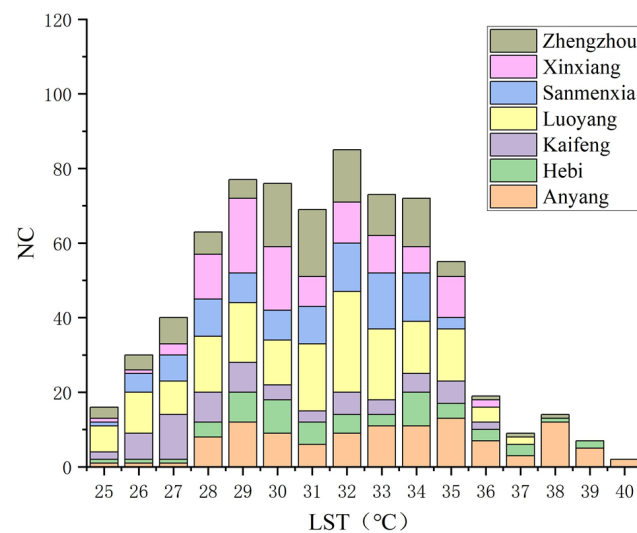
Figure 13. Distribution curves of attribute information of connected regions in different districts on five dates: (**a**) number of connected regions, (**b**) regional fragmentation, (**c**) average LST, (**d**) average NDVI, (**e**) average NDBI, (**f**) CC_TV, and (**g**) CC_TB.

The analysis results of the changes in the average LSTs, land-object-type indexes, and correlation coefficients of each city follow. As shown in Figure 11c, from 15 May 2006 to 1 May 2010, the average LST of Xinxiang, Hebi, and Sanmenxia decreased slightly, while that of the other cities increased. On 1 May 2010, only the average LST of Anyang city exceeded 37 °C. From 1 May 2010 to 7 May 2014, the average LST of Anyang, Hebi, and Sanmenxia decreased, and that of the other cities increased to varying degrees. From 7 May 2014 to 29 April 2017, the average LST of Zhengzhou and Kaifeng decreased, and the average LST of the other cities increased. From 29 April 2017 to 8 May 2021, the average LST of Zhengzhou and Luoyang increased, and that of the other cities decreased. From 1 May 2010 to 8 May 2021, the average temperature of every city was above 36 °C, among which Anyang had the highest average LST and Sanmenxia the lowest. As shown in Figure 13d, from 15 May 2006 to 1 May 2010, the average NDVI values of Zhengzhou, Kaifeng, and Luoyang decreased, and that of the other cities increased. On 1 May 2010, only Zhengzhou had an average NDVI value less than 0.3 and was the lowest of the five dates. From 1 May 2010 to 7 May 2014, the average NDVI values of Anyang, Hebi, and Sanmenxia decreased, and those of the other cities increased. From 7 May 2014 to 29 April 2017, the average NDVI value for all cities increased. From 29 April 2017 to 8 May 2021, except for Kaifeng, Anyang, and Hebi, the average NDVI values of cities increased to varying degrees. In addition, from 15 May 2006 to 8 May 2021, Zhengzhou and Luoyang had the largest changes in the average NDVI. As shown in Figure 13e, from 15 May 2006 to 1 May 2010, for all cities except Kaifeng and Hebi, the average NDBI decreased. From 1 May 2010 to 7 May 2014, the average NDBI of all cities decreased except for Anyang. From 7 May 2014 to 29 April 2017, the average NDBI in Zhengzhou increased, while that of the other cities decreased. From 29 April 2017 to 8 May 2021, for all cities except Luoyang and Sanmenxia, the average NDBI increased, while the average NDBI of Luoyang and Sanmenxia continued to decline, and Luoyang had the lowest average NDBI of all cities since 7 May 2014. Figure 13f shows the changes in the CC_TVs. From 15 May 2006 to 7 May 2014, the CC_TVs of Zhengzhou, Luoyang, and Hebi first increased and then decreased, that of Kaifeng and Anyang City first decreased and then increased, while that of Xinxiang and Sanmenxia continued to increase. From 7 May 2014 to 8 May 2021, the CC_TVs of Zhengzhou, Hebi, and Sanmenxia first increased and then decreased; those of Luoyang, Xinxiang, and Kaifeng first decreased and then increased; and that of Anyang continued to decrease. Figure 13g shows the changes in the CC_TBs. From 15 May 2006 to 7 May 2014, the CC_TBs of Zhengzhou, Luoyang, Xinxiang, and Hebi first decreased and then increased, those of Kaifeng and Anyang first increased and then decreased, and that of Sanmenxia continued to decrease. From 7 May 2014 to 8 May 2021, the CC_TBs of Zhengzhou, Hebi, and Sanmenxia first decreased and then increased; those of Luoyang, Xinxiang, and Kaifeng first increased and then decreased; and that of Anyang continued to increase.
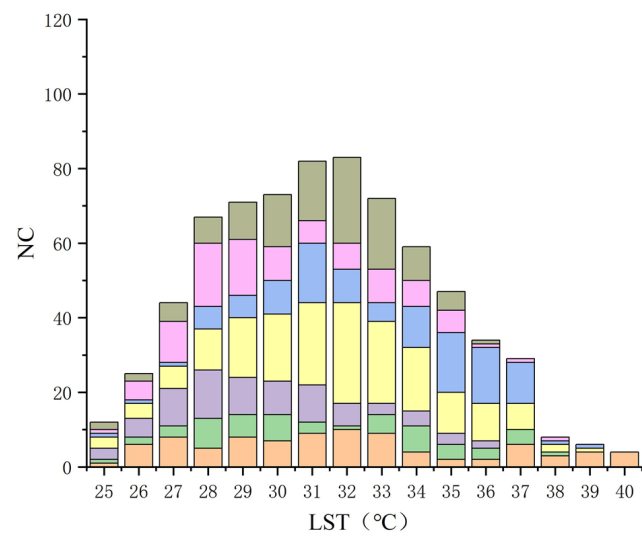
To analyze the temperature changes in the seven cities, the LST data were counted as a tree structure. Figure 14a–e represents the tree structure information of the cities on five dates. The abscissa represents the hierarchical level of the tree structure; that is, the longitudinal depth of a city's temperature center. The ordinate represents the number of nodes on each level of the tree structure; that is, the number of urban temperature centers. Figure 14a,b shows that in 2006 and 2010, respectively, the number of temperature centers in the cities first increased and then decreased, and the number of temperature centers reached a maximum value of 32 °C. Among them, Luoyang had the largest number of temperature centers, indicating that Luoyang has more temperature radiation centers, and the surface temperature easily diffused. The number of temperature centers in Anyang was relatively small, but the longitudinal depth of the temperature center was the largest, indicating that high-temperature areas existed in the temperature center of Anyang. Figure 14c,d shows that in 2014 and 2017, respectively, the number of low-temperature (below 28 °C) areas in the cities began to decrease, the temperature level increased when the number of temperature centers peaked, and the depth of the temperature centers in many cities

increased. The rising average LSTs from 2014 to 2017 shown in Table 3 shows that cities began to warm up and produced a greater number of high-temperature regional centers. As shown in Figure 14e, compared with the other years, the number of temperature centers in the cities in 2021 decreased but changed little at different temperature levels. The number of low-temperature centers increased, and the number of cities whose temperature centers reached 40 °C decreased, which is consistent with the decrease in the average LST from 2017 to 2021 in Table 3.
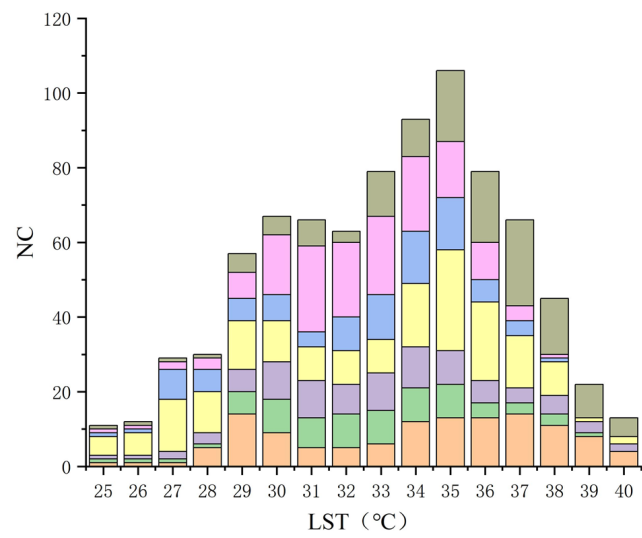
As shown in Table 5, Crosswise Max (CM) represents the maximum value of the connected area of each city at different temperature levels; that is, the temperature level had the highest-temperature center values, and Lengthwise Max (LM) represents the maximum number of temperature center layers. In 2006, 2010, and 2014, the maximum number of temperature centers in Zhengzhou, Luoyang, and Xinxiang were larger and showed an increasing trend over time, while those of other cities were smaller. In 2017, Luoyang, Xinxiang, and Sanmenxia had the largest number of temperature centers, all of which were greater than 20, while other cities had relatively few. In 2021, Anyang, Luoyang, Sanmenxia, and Xinxiang had large maximum numbers of temperature centers, while other cities had smaller numbers. From 2014 to 2021, the maximum number of temperature centers in Zhengzhou showed a downwards trend because, combined with the image-map results of Figure 8, the area of temperature-connected regions in Zhengzhou gradually became larger and relatively compact. In addition, the maximum number of temperature centers in Hebi was always lower than that in other cities because the administrative area of Hebi is relatively small. On the five study dates, the maximum number of temperature-center layers in the seven cities was greater than 11; that is, there were high temperature areas above 35 °C. In 2014 and 2017, the maximum number of layers in the temperature centers was generally larger, and there were significantly more cities, reaching 16; that is, the temperature areas reaching 40 °C began to increase, indicating that the temperatures in the cities increased during this period.
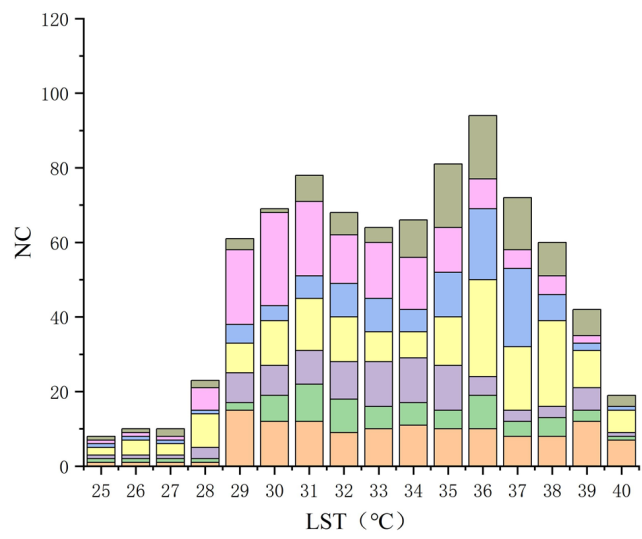

(a)

Figure 14. *Cont.*

(b)

(c)
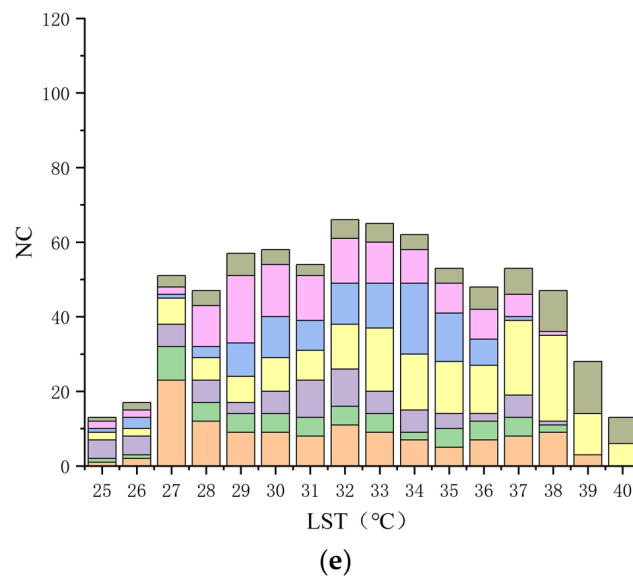

(d)

Figure 14. *Cont.*

(e)

Figure 14. Histogram of tree structure information in different regions on five dates: (**a**) 15 May 2006, (**b**) 1 May 2010, (**c**) 7 May 2014, (**d**) 29 April 2017, and (**e**) 8 May 2021.

Table 5. Tree structure analysis of cities.

Date	City＼Direction	Anyang	Hebi	Kaifeng	Luoyang	Sanmenxia	Xinxiang	Zhengzhou
2006-05-15	CM	13	9	12	27	15	20	18
	LM	16	15	12	13	11	12	14
2010-05-01	CM	10	8	13	27	16	17	23
	LM	16	14	12	15	15	14	12
2014-05-07	CM	14	9	11	27	14	23	30
	LM	16	15	16	16	14	14	16
2017-04-29	CM	15	10	12	26	21	25	17
	LM	16	16	16	16	16	15	16
2021-05-08	CM	23	9	10	23	19	18	14
	LM	15	14	14	16	13	14	16

5. Conclusions

This study used MODIS data from different years as data sources to obtain and analyze LST data and LST index information for Henan Province. Connectivity analysis was performed at different temperature levels to calculate the number and sizes of connected areas, temperature and ground-type index values, and other attribute information. Based on the multigrade analysis of the LST data in Henan Province over different years, an MTML analysis method was developed.

Taking Henan Province, China, as the study area, the LST in the study area was obtained from MODIS data for 15 May 2006, 1 May 2010, 7 May 2014, 29 April 2014, and 8 May 2021. The generated LST data were processed to generate different connected regions at different temperature levels, and the regional attribute information of all connected regions at the 25–40 °C temperature level was statistically analyzed. Data analysis shows that from 2006 to 2010, the NDVI increased and the LST decreased in Henan Province. From 2010 to 2014, the decrease in the NDVI led to an increase in the LST in Henan Province. From 2014 to 2017, the NDVI increased in Henan Province, but the impact of the greenhouse effect may have led to an increase in the LST. From 2017 to 2021, the increase in the NDVI in Henan Province led to a decrease in the LST. Through an analysis of the number of connected areas and fragmentation degree of each temperature grade in Henan Province, it

was found that the minimum peak value and maximum fragmentation degree of connected areas occurred in 2006, the maximum peak value of connected areas occurred in 2021, and the minimum fragmentation degree in 2021 was almost lower than that in 2017. This indicates that there were fewer high-temperature areas in 2006 and a greater number of high-temperature areas in 2021. In addition, the influence of the size of connected areas was discussed, and the results showed that with an increase in the area size, the average LST changed within 1 °C and presented a gradually rising trend, while the average NDVI and average NDBI changed little.

The regional number, regional fragmentation, average LST, average NDVI, average NDBI, and correlation coefficients of connected areas with high temperatures (above 35 °C) in seven cities in Henan Province were statistically analyzed. The results showed that Luoyang, Sanmenxia, and Xinxiang have a large number of high-temperature connected areas; whereas Anyang, Zhengzhou, and Kaifeng have a relatively small number; and Hebi has the leas. An analysis of the temperature changes in seven cities by constructing tree structures showed that the number of cities with high temperatures of 40 °C in 2014 and 2017 was significantly greater than in the other years of this study.

Author Contributions: Conceptualization, Z.Z., B.S., G.C. and C.W.; methodology, Z.Z., B.S. and G.C.; validation, Z.Z. and B.S.; formal analysis, Z.Z., B.S., G.C., C.W. and N.Y.; investigation, Z.Z., B.S. and G.C.; resources, Z.Z. and B.S.; data curation, Z.Z., B.S. and N.Y.; writing—original draft preparation, Z.Z., B.S., H.W. and X.T.; writing—review and editing, Z.Z., B.S., H.W. and X.T. All authors have read and agreed to the published version of the manuscript.

Institutional Review Board Statement: Not applicable.

Informed Consent Statement: Not applicable.

Data Availability Statement: Not applicable.

Conflicts of Interest: The authors declare no conflict of interest.

References

1. Peng, J.; Xie, P.; Liu, Y.X.; Ma, J. Urban thermal environment dynamics and associated landscape pattern factors: A case study in the Beijing metropolitan region. *Remote Sens. Environ.* **2016**, *173*, 145–155. [CrossRef]
2. National Bureau of Statistics. *China Statistics Yearbook*; China Statistics Press: Beijing, China, 2021.
3. Jenerette, G.D.; Harlan, S.L.; Stefanov, W.L.; Martin, C.A. Ecosystem services and urban heat riskscape moderation: Water, green spaces, and social inequality in Phoenix, USA. *Ecol. Appl.* **2011**, *21*, 2637–2651. [CrossRef] [PubMed]
4. Du, S.H.; Xiong, Z.Q.; Wang, Y.C.; Guo, L. Quantifying the multilevel effects of landscape composition and configuration on land surface temperature. *Remote Sens. Environ.* **2016**, *178*, 84–92. [CrossRef]
5. Lu, L.; Weng, Q.; Xiao, D.; Guo, H.; Hui, W. Spatiotemporal Variation of Surface Urban Heat Islands in Relation to Land Cover Composition and Configuration: A Multi-Scale Case Study of Xi'an, China. *Remote Sens.* **2020**, *12*, 2713. [CrossRef]
6. Shahfahad; Rihan, M.; Naikoo, M.W.; Ali, M.A.; Rahman, A. Urban Heat Island Dynamics in Response to Land-Use/Land-Cover Change in the Coastal City of Mumbai. *J. Indian Soc. Remote Sens.* **2021**, *49*, 2227–2247. [CrossRef]
7. Yao, L.; Sun, S.; Song, C.; Li, J.; Xu, Y. Understanding the spatiotemporal pattern of the urban heat island footprint in the context of urbanization, a case study in Beijing, China. *Appl. Geogr.* **2021**, *133*, 102496. [CrossRef]
8. Rizwan, A.M.; Dennis, Y.C.L.; Liu, C.H. A review on the generation, determination and mitigation of Urban Heat Island. *J. Environ. Sci.* **2008**, *20*, 120–128. [CrossRef]
9. Zhou, W.Q.; Wang, J.; Cadenasso, M.L. Effects of the spatial configuration of trees on urban heat mitigation: A comparative study. *Remote Sens. Environ.* **2017**, *195*, 1–12. [CrossRef]
10. Li, H.D.; Zhou, Y.Y.; Wang, X.; Zhou, X.; Zhang, H.W.; Sodoudi, S. Quantifying urban heat island intensity and its physical mechanism using WRF/UCM. *Sci. Total Environ.* **2019**, *650*, 3110–3119. [CrossRef]
11. Manley, G. On the Frequency of Snowfall in Metropolitan England. *Q. J. R. Meteorol. Soc.* **1958**, *84*, 70–72. [CrossRef]
12. Deosthali, V. Impact of rapid urban growth on heat and moisture islands in Pune City, India. *Atmos. Environ.* **2000**, *34*, 2745–2754. [CrossRef]

13. Saaroni, H.; Ben-Dor, E.; Bitan, A.; Potchter, O. Spatial distribution and microscale characteristics of the urban heat island in Tel-Aviv, Israel. *Landsc. Urban Plan.* **2000**, *48*, 1–18. [CrossRef]

14. Kim, Y.-H.; Baik, J.-J. Maximum Urban Heat Island Intensity in Seoul. *J. Appl. Meteorol.* **2002**, *41*, 651–659. [CrossRef]

15. Giridharan, R.; Ganesan, S.; Lau, S.S.Y. Daytime urban heat island effect in high-rise and high-density residential developments in Hong Kong. *Energy Build.* **2004**, *36*, 525–534. [CrossRef]

16. Rao, P.K. Remote sensing of urban heat islands from an environmental satellite. *Bull. Am. Meteorol. Soc.* **1972**, *53*, 647–648.

17. Sobrino, J.A.; Jimenez-Munoz, J.C.; Soria, G.; Romaguera, M.; Guanter, L.; Moreno, J.; Plaza, A.; Martincz, P. Land surface emissivity retrieval from different VNIR and TIR sensors. *IEEE Trans. Geosci. Remote Sens.* **2008**, *46*, 316–327. [CrossRef]

18. Li, J.J.; Wang, X.R.; Wang, X.J.; Ma, W.C.; Zhang, H. Remote sensing evaluation of urban heat island and its spatial pattern of the Shanghai metropolitan area, China. *Ecol. Complex.* **2009**, *6*, 413–420. [CrossRef]

19. Li, Y.Y.; Zhang, H.; Kainz, W. Monitoring patterns of urban heat islands of the fast-growing Shanghai metropolis, China: Using time-series of Landsat TM/ETM+ data. *Int. J. Appl. Earth Obs. Geoinf.* **2012**, *19*, 127–138. [CrossRef]

20. Jimenez-Munoz, J.C.; Sobrino, J.A.; Skokovic, D.; Mattar, C.; Cristobal, J. Land Surface Temperature Retrieval Methods from Landsat-8 Thermal Infrared Sensor Data. *IEEE Geosci. Remote Sens. Lett.* **2014**, *11*, 1840–1843. [CrossRef]

21. Chen, M.; Zhou, Y.; Hu, M.; Zhou, Y. Influence of Urban Scale and Urban Expansion on the Urban Heat Island Effect in Metropolitan Areas: Case Study of Beijing-Tianjin-Hebei Urban Agglomeration. *Remote Sens.* **2020**, *12*, 3491. [CrossRef]

22. Yang, J.; Zhan, Y.; Xiao, X.; Xia, J.C.; Li, X. Investigating the diversity of land surface temperature characteristics in different scale cities based on local climate zones. *Urban Clim.* **2020**, *34*, 100700. [CrossRef]

23. Cui, F.; Hamdi, R.; Yuan, X.; He, H.; Maeyer, P.D. Quantifying the response of surface urban heat island to urban greening in global north megacities. *Sci. Total Environ.* **2021**, *801*, 149553. [CrossRef]

24. Song, Z.; Yang, H.; Huang, X.; Yu, W.; Huang, J.; Ma, M. The spatiotemporal pattern and influencing factors of land surface temperature change in China from 2003 to 2019. *Int. J. Appl. Earth Obs. Geoinf.* **2021**, *104*, 102537. [CrossRef]

25. Guo, M.; Chen, S.; Wang, W.; Liang, H.; Hao, G.; Liu, K. Spatiotemporal variation of heat fluxes in Beijing with land use change from 1997 to 2017. *Phys. Chem. Earth* **2019**, *110*, 51–60. [CrossRef]

26. Hawkins, T.W.; Brazel, A.J.; Stefanov, W.L.; Bigler, W.; Saffell, E.M. The role of rural variability in urban heat island determination for Phoenix, Arizona. *J. Appl. Meteorol.* **2004**, *43*, 476–486. [CrossRef]

27. Chen, X.L.; Zhao, H.M.; Li, P.X.; Yin, Z.Y. Remote sensing image-based analysis of the relationship between urban heat island and land use/cover changes. *Remote Sens. Environ.* **2006**, *104*, 133–146. [CrossRef]

28. Duan, S.B.; Li, Z.L.; Tang, B.H.; Wu, H.; Tang, R.L. Generation of a time-consistent land surface temperature product from MODIS data. *Remote Sens. Environ.* **2014**, *140*, 339–349. [CrossRef]

29. Estoque, R.C.; Murayama, Y.; Myint, S.W. Effects of landscape composition and pattern on land surface temperature: An urban heat island study in the megacities of Southeast Asia. *Sci. Total Environ.* **2017**, *577*, 349–359. [CrossRef]

30. The People's Government of Henan Province. *Provincial Situation*; Henan Daily News Group Co., Ltd.: Zhengzhou, China, 2021.

31. Wan, Z.; Zhang, Y.; Zhang, Q.; Li, Z.L. Validation of the land-surface temperature products retrieved from Terra Moderate Resolution Imaging Spectroradiometer data. *Remote Sens. Environ.* **2002**, *83*, 163–180. [CrossRef]

32. Fu, H. Spatial-Temporal Reconstruction and Analysis of Dynamic Driving Factors for Land Surface Temperatures in Urban Area. Ph.D. Thesis, Wuhan University, Wuhan, China, 2020.

33. Ji, R. Temporal and Spatial Variation of Surface Temperature and Influencing Factors Analysis in Liaoning Province from 1960 to 2016. Master's Thesis, Liaoning Normal University, Dalian, China, 2018.

34. Purevdorj, T.; Tateishi, R.; Ishiyama, T.; Honda, Y. Relationships between percent vegetation cover and vegetation indices. *Int. J. Remote Sens.* **1998**, *19*, 3519–3535. [CrossRef]

35. Zha, Y.; Gao, J.; Ni, S. Use of normalized difference built-up index in automatically mapping urban areas from TM imagery. *Int. J. Remote Sens.* **2003**, *24*, 583–594. [CrossRef]

36. Salembier, P.; Oliveras, A.; Garrido, L. Antiextensive connected operators for image and sequence processing. *IEEE Trans. Image Processing A Publ. IEEE Signal Processing Soc.* **1998**, *7*, 555–570. [CrossRef] [PubMed]

37. Braga-Neto, U.; Goutsias, J. Connectivity on Complete Lattices: New Results. *Comput. Vis. Image Underst.* **2002**, *85*, 22–53. [CrossRef]

38. Zhao, Z.; Cheng, G.; Wang, C.; Wang, S.; Wang, H. City Grade Classification Based on Connectivity Analysis by Luojia I Night-Time Light Images in Henan Province, China. *Remote Sens.* **2020**, *12*, 1705. [CrossRef]

39. Hobbs, R.J. Effects of landscape fragmentation on ecosystem processes in the Western Australian wheatbelt. *Biol. Conserv.* **1993**, *64*, 193–201. [CrossRef]